

Article

C₆₀- and CdS-Co-Modified Nano-Titanium Dioxide for Highly Efficient Photocatalysis and Hydrogen Production

Meifang Zhang ¹, Xiangfei Liang ^{1,*}, Yang Gao ¹ and Yi Liu ^{2,*} 

¹ Institute of Carbon Neutral New Energy Research, Yuzhang Normal University, Nanchang 330031, China; mfzhang@whu.edu.cn (M.Z.); ygao2023@126.com (Y.G.)

² School of Chemical and Environmental Engineering, Wuhan Polytechnic University, Wuhan 430023, China

* Correspondence: xliang96@126.com (X.L.); yiliu@whu.edu.cn (Y.L.)

Abstract: The inherent properties of TiO₂, including a wide band gap and restricted spectral response range, hinder its commercial application and its ability to harness only 2–3% of solar energy. To address these challenges and unlock TiO₂'s full potential in photocatalysis, C₆₀- and CdS-co-modified nano-titanium dioxide has been adopted in this work to reduce the band gap, extend the absorption wavelength, and control photogenerated carrier recombination, thereby enhancing TiO₂'s light-energy-harnessing capabilities and hydrogen evolution capacity. Using the sol-gel method, we successfully synthesized CdS-C₆₀/TiO₂ composite nanomaterials, harnessing the unique strengths of CdS and C₆₀. The results showed a remarkable average yield of 34.025 μmol/h for TiO₂ co-modified with CdS and C₆₀, representing a substantial 17-fold increase compared to pure CdS. Simultaneously, the average hydrogen generation of C₆₀-modified CdS surged to 5.648 μmol/h, a notable two-fold improvement over pure CdS. This work opens up a new avenue for the substantial improvement of both the photocatalytic degradation efficiency and hydrogen evolution capacity, offering promise of a brighter future in photocatalysis research.

Keywords: co-modified; CdS-C₆₀/TiO₂; photocatalytic activity; hydrogen evolution



Citation: Zhang, M.; Liang, X.; Gao, Y.; Liu, Y. C₆₀- and CdS-Co-Modified Nano-Titanium Dioxide for Highly Efficient Photocatalysis and Hydrogen Production. *Materials* **2024**, *17*, 1206. <https://doi.org/10.3390/ma17051206>

Academic Editor: Ovidiu Oprea

Received: 18 December 2023

Revised: 6 February 2024

Accepted: 8 February 2024

Published: 5 March 2024



Copyright: © 2024 by the authors. Licensee MDPI, Basel, Switzerland. This article is an open access article distributed under the terms and conditions of the Creative Commons Attribution (CC BY) license (<https://creativecommons.org/licenses/by/4.0/>).

1. Introduction

In recent years, photocatalytic technology has garnered significant attention from researchers owing to its cost-effectiveness, simplicity, and minimal environmental impact. This versatile technology leverages a range of photocatalysts to disintegrate a wide array of both organic and inorganic pollutants, offering the promise of converting CO₂ into valuable renewable chemicals and facilitating water decomposition [1–3]. Among these photocatalysts, titanium dioxide (TiO₂) stands out for its relatively high activity, rendering it highly effective in the purification of air and water, even in biomedical applications [4,5]. Consequently, its applications in the field of photocatalysis hold considerable promise [6,7].

Nevertheless, the inherent limitations of TiO₂ are its wide band gap and restricted spectral response range, which result in its ability to utilize only approximately 2–3% of solar energy and hinder its commercial application [8]. To address these challenges and unlock the full potential of TiO₂ in photocatalysis, modification techniques have emerged as a pivotal approach to enhancing its photocatalytic performance. These techniques aim to reduce the band gap, extend the absorption wavelength, and control photogenerated carrier recombination, thereby enhancing TiO₂'s light-energy-harnessing capabilities [9]. Notably, the choice of dopants significantly influences the photocatalytic activity, affecting the recombination of photogenerated electrons (e⁻) and holes (h⁺) on the material's surface.

In the field of photoelectrochemical water decomposition, nano-TiO₂ coupling systems have been extensively researched [10,11]. Cadmium sulfide (CdS), with its narrow energy gap of 2.4 eV, has proved effective as a coupling agent for TiO₂, promoting the photocatalytic decomposition of water [12,13]. The strong coupling between TiO₂ and CdS allows for

the direct combination of TiO₂ particles with dispersed CdS particles. Although CdS exhibits photoetching instability when used independently, the formation of composite nanomaterials with TiO₂, characterized by a wider band gap, effectively reduces the likelihood of photogenerated electron–hole recombination. Thus, the strategic coupling of TiO₂ with CdS mitigates the photoetching instability associated with CdS alone and expands the spectral response range [14–16].

Fullerene (C₆₀), renowned for its exceptional electron (e[−]) transport capabilities, has emerged as an intriguing option for mitigating charge recombination. This has fueled increasing interest in TiO₂ catalysts supported by C₆₀ [17,18]. C₆₀ boasts an extensive three-dimensional π electron system, featuring a closed core–shell structure comprising 60 delocalized π electrons and 30 bonded molecular orbitals. Even minor structural variations or changes in the solvent properties can influence the electron transfer within the system, making the incorporation of C₆₀ an attractive strategy for enhancing effective electron transfer [19,20]. With a band gap ranging from 1.6 to 1.9 eV, C₆₀ holds considerable promise for practical applications, and catalysts modified with C₆₀ are poised to achieve a remarkable photocatalytic performance.

Recognizing the complementary advantages of CdS and C₆₀, we have adopted a comprehensive approach to co-modifying TiO₂. Utilizing the sol-gel method, we have successfully synthesized CdS-C₆₀/TiO₂ composite nanomaterials with highly effective photocatalytic properties. Remarkably, the hydrogen production of CdS modified with C₆₀ exhibited a two-fold increase compared to pure CdS, reaching an average of 5.648 $\mu\text{mol/h}$. Furthermore, TiO₂ co-modified with CdS and C₆₀ demonstrated an impressive average yield of 34.025 $\mu\text{mol/h}$, representing a staggering 17-fold increase over pure CdS. This study underscores the synergistic benefits of combining CdS and C₆₀ in enhancing the photocatalytic and hydrogen production performance of TiO₂, opening up new avenues for sustainable and efficient environmental remediation processes.

2. Materials and Methods

Materials: The cadmium chloride (CdCl₂, 99.0%) and sodium sulfide (Na₂S·9H₂O) were purchased from Tianjin Kemiou Chemical Reagent Co., Ltd. (Tianjin, China). The Malachite Green (MG), P25 (Degussa, Hamburg, Germany), and butyl titanate (Ti(OBu)₄) were all purchased from China National Pharmaceutical Group Chemical Reagent Co., Ltd. (Beijing, China). The C₆₀ was purchased from Shanghai Macklin Biochemical Co., Ltd. (Shanghai, China). All the other reagents were analytical-grade. The pH of the solution was adjusted using nitric acid and sodium hydroxide solutions. All experiments used secondary water.

Synthesis of CdS: Dissolve 3.1148 g of CdCl₂·2.5H₂O in 20 mL of ethanol in the first bottle, and dissolve 2.4004 g of Na₂S·9H₂O in 20 mL of ethanol in the second bottle. After stirring for 10 min, the second bottle is added to the first bottle slowly, drop by drop. Gel A is stirred for two hours at room temperature before being transferred into an alumina crucible. Place the sample into a muffle furnace and set the conditions to increase from room temperature to 450 °C, with a heating rate of 2 °C/min in an air atmosphere, and maintain it there for 2 h after aging at room temperature for 24 h. The calcination conditions are the same for each sample below. Finally, create a sample of CdS powder by grinding the acquired sample in an agate mortar [21–23].

Synthesis of CdS-TiO₂: Make gel A as directed by the conditions listed above. In a flask with a circular bottom and labeled “gel B”, combine 20 mL of butyl titanate (TBT) with 30 mL of ethanol solution. The combination added dropwise is stirred at room temperature for 2 h. Prepare another combination using 20 mL of ethanol, 4 mL of distilled water, 2 mL of nitric acid, and 20 mL of gel A. They should be added dropwise to the room-temperature gel B solution, stirred as they are added, and left to react for 24 h. Age for 24 h in an alumina crucible. The sample is burned under the same conditions in a muffle furnace and then ground to produce a CdS-TiO₂ sample.

Synthesis of CdS-C₆₀: In order to create CdS, 30 mg of Ox-C₆₀ (also known as activated C₆₀) is added to a combination of distilled water and agitated for 2 h. An alumina crucible is used to age gel C for 24 h. Then, under the same conditions, it is calcined in a muffle furnace. The CdS-C₆₀ sample is obtained by grinding it after cooling to room temperature.

Synthesis of CdS-C₆₀-TiO₂: Synthesize gel B and gel C separately, measure 20 mL of ethanol and 4 mL of distilled water, and combine 2 mL of nitric acid and gel C to put together another mixture. The combination dropwise is added to the gel B solution at room temperature, stir whilst adding, and react for 24 h. Age it in an alumina crucible for 24 h and burn it in a muffle furnace underneath the identical conditions. Grind to achieve the CdS-C₆₀-TiO₂ sample. The experimental characterization is detailed in the Supporting Information (pages 2–4).

3. Results and Discussion

To explore the changes in the TiO₂ crystal morphology after the modification, we conducted X-ray diffraction (XRD) measurements for the pure TiO₂ and the modified TiO₂ materials in Figure 1a. As can be seen, the diffraction peaks of P25 (commercial TiO₂) appear at $2\theta = 25.08^\circ, 37.94^\circ, 48.14^\circ, 54.26^\circ, 55.26^\circ, 62.90^\circ, 68.98^\circ, 70.02^\circ,$ and 75.24° , respectively, corresponding to the diffraction peaks of anatase-phase TiO₂ (101), (004), (200), (105), (211), (204), (116), (200), and (215), respectively, where $2\theta = 25.08^\circ$ was the strongest diffraction peak. The diffraction peaks of the rutile phase (110), (101), and (200) crystal faces appear at $2\theta = 27.7^\circ, 36.2^\circ,$ and 42.82° , indicating that TiO₂ is a mixed crystal structure dominated by anatase phases and rutile phases [24]. Comparing P25, CdS-TiO₂, and CdS-C₆₀/TiO₂, the rutile diffraction peak weakened in turn, and the anatase-phase diffraction peak increased in turn, indicating that the introduction of CdS into the samples can inhibit the growth of their rutile phase. As we all know, rutile TiO₂, as the most stable crystalline structure form, has a good crystallization state and fewer defects, resulting in electrons and holes that are easy to compound, with almost no photocatalytic activity. Therefore, the CdS-C₆₀/TiO₂ composite with less rutile TiO₂ will have a better catalytic performance. We also tested the XPS patterns of P25, CdS-TiO₂, and CdS-C₆₀/TiO₂, as shown in Figure S1 (Supporting Information). It was proven that there is no Ti2p separation between the C₆₀, CdS, and TiO₂ phases after preparation, but the shift in the oxygen atom toward a high binding energy means that the chemical bonds between the oxygen atom and other elements become tighter and more stable, which indicates that CdS-C₆₀ has a significant effect on the modification of TiO₂, which promotes the transfer of electrons between oxygen atoms and other elements, thereby increasing the activity of the catalyst.

Not only that but most UV radiation with a wavelength of less than 400 nm is absorbed by P25. The absorption bands of CdS, CdS-C₆₀, CdS-TiO₂, and CdS-C₆₀/TiO₂ all entered the visible light region. This is mainly because the band gap of CdS is 2.4 eV, the response characteristics of visible light are better, and the crystal structure of the original substance is changed after being modified with CdS. Compared with pure CdS and pure TiO₂, the absorbance of CdS-C₆₀ and CdS-C₆₀/TiO₂ increased, showing that the band gaps of various semiconductor catalysts overlapped in the ultraviolet and visible regions, respectively, which is conducive to improving their photocatalytic performance. The C₆₀-modified sample's absorption band edge shows some redshift, indicating that C₆₀ can narrow the catalyst's band gap, which is due to the interaction between the components, causing surface lattice oxygen vacancy and other defects [25–27]. The results above indicate that the crystal structure of TiO₂ is alterable by CdS and C₆₀, leading to the creation of defects on the surface lattice. The cause of the edge absorption is the defect absorption rather than the actual absorption of the lattice [28]. Additionally, the band gap energy of TiO₂ is decreased, enabling it to be activated by visible light and to exhibit photocatalytic activity. These changes not only enhance the utilization of light energy but also improve the overall efficiency of the photocatalysis process. Meanwhile, EDX fluorescence spectroscopy analyses on each sample were performed to detect the type and content of the characteristic elements contained in each sample, as shown in Figure 1c–e.

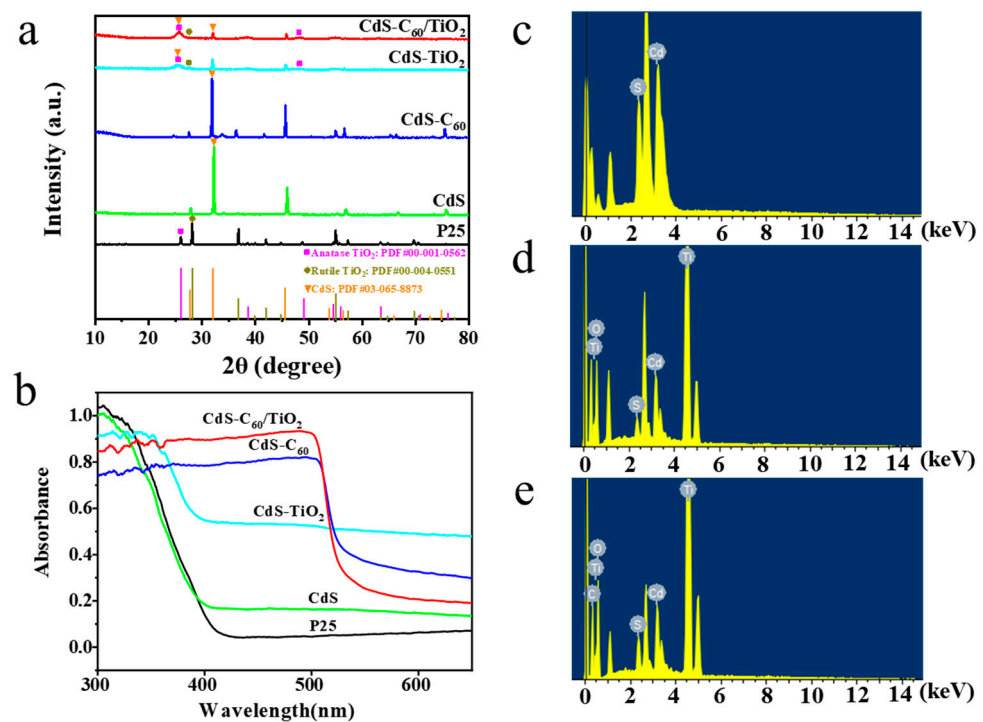


Figure 1. (a) XRD patterns and (b) UV-Vis diffuse reflectance spectra of P25, CdS, CdS-C₆₀, CdS-TiO₂, and CdS-C₆₀/TiO₂. Energy-Dispersive X-ray (EDX) elemental microanalysis of (c) CdS, (d) CdS-TiO₂, (e) CdS-C₆₀/TiO₂.

As the FT-IR spectra show in Figure 2a,b, all the catalyst samples have strong absorption peaks at 3420–3510 cm⁻¹ and 1620–1640 cm⁻¹, corresponding to the bending vibration peaks of the H-O-H bonds, which indicates the bending vibration of the presence of numerous water molecules adsorbed onto the catalyst surface. These peaks confirm that water molecules adhere to the catalyst surface in a physical manner. Consequently, it can be concluded that these nanomaterials possess the ability to exhibit a significant photocatalytic effect, which may be the presence of the majority of hydroxyl groups on the surface, and under photoexcitation, the e⁻-h⁺ pair generated by the catalyst sample acts on the hydroxyl group to generate highly oxidizing ·OH. The abundant and diverse hydroxyl groups present on the surface also promote the creation of sites where O₂, CO₂, and CO molecules can be adsorbed [29]. The absorption peak at 1380 cm⁻¹ of the spectrum indicates that O₂ molecules are adsorbed on the surface. Whether it is the formation of highly oxidizing free radicals or the provision of adsorption sites for small molecules, this facilitates the oxidation of organic material into a variety of small molecule compounds via photocatalysis. In comparison to P25, the absorption peaks of CdS-TiO₂ and CdS-C₆₀/TiO₂ shift toward higher frequencies. The peak at 450–510 cm⁻¹ signifies the presence of titanate TiO₃²⁻, indicating that the transition of TiO₂ involves lattice distortion [30]. It can be deduced that the periodic potential field distortion generated by the modification of CdS and C₆₀ caused lattice defects in the TiO₂. The TiO₂ band gap decreases, leading to an enhanced ability to catalyze visible light. Although the sample contains a small amount of titanate TiO₃²⁻, the photocatalytic activity can be effectively improved by introducing more crystal defects [31]. The band of CdS-C₆₀-TiO₂ changes the lattice to produce some characteristic peaks at 1380 cm⁻¹, which further indicates that CdS, C₆₀, and TiO₂ are bonded, changing the original lattice structure of the TiO₂. It may be inferred from band analyses of CdS, CdS-C₆₀, CdS-TiO₂, and CdS-C₆₀/TiO₂ that the same absorption peak, which may represent a Cd-S bond vibration, is present in all of these materials.

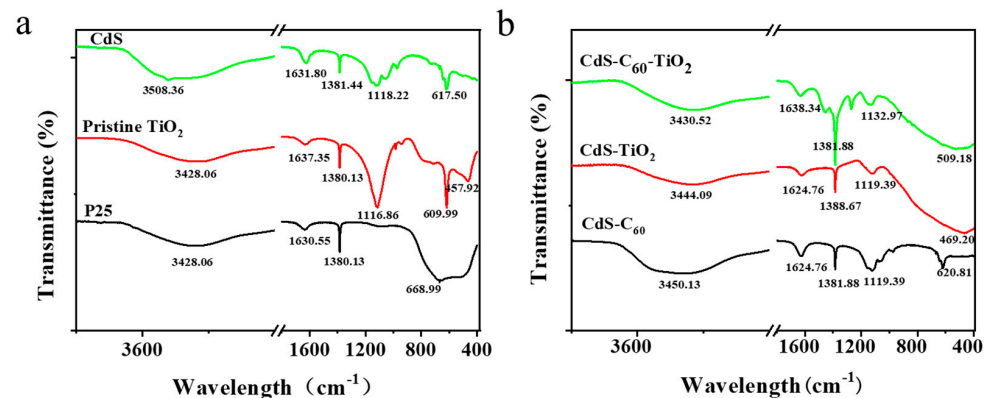


Figure 2. (a) FT-IR spectra of P25, pristine TiO₂, CdS, (b) CdS-C₆₀, CdS-TiO₂, and CdS-C₆₀-TiO₂.

Since the photocatalytic activity of the functionalized materials is largely dependent on their morphological structure, it can be found that P25 (Figure S2a,b, Supporting Information) is a solid microsphere. However, after being modified by CdS, the particles become less uniform, and as seen using XRD, there is an interaction between CdS and TiO₂, making its crystal lattice larger. CdS and C₆₀ uniformly cover the surface of TiO₂ in the form of lumps and microspheres, and the aggregation of small particles aggravates the surface roughness (Figure S2c–j, Supporting Information), as is consistent with the results of SEM. By comparing the TEM of the samples CdS-TiO₂ (Figure S3a, Supporting Information) and CdS-C₆₀/TiO₂ (Figure S3b, Supporting Information), we see the crystal plane of the CdS-C₆₀/TiO₂ composite is clearer and regular, the crystal form is more perfect, and the lattice fringes of TiO₂ and CdS can be seen clearly. This indicates that the introduction of C₆₀ changed the lattice structure of TiO₂, making the crystal form better. In addition, the connection between the suitable specific surface area and the variables affects the sample's photocatalytic performance. We calculated the pore size and pore distribution of each sample using the Barrett–Joyner–Halenda technique and the Halsey equation, as shown in Table S1 (Supporting Information) [32–34]. From the nitrogen adsorption data of the six catalyst samples, when compared to CdS, the specific surface area of CdS-TiO₂ has increased in comparison to commercial P25 and CdS-C₆₀, but the rate of the change in the pore size is much greater than the change in the specific surface area. This may be a result of the dopant entering the lattice and causing the pore size to decrease, conducive to producing lattice defects in the crystal structure. This improves the photocatalytic activity [35]. As a product of CdS and C₆₀ co-modification, in CdS-C₆₀/TiO₂, it is hypothesized that the factors influencing the photocatalytic performance of the sample are related to an appropriate specific surface area and a certain degree of lattice defects. As the specific surface area increases, so does the number of active sites, leading to the higher adsorption performance of the catalyst. Conversely, reducing the specific surface area leads to a decrease in both the pore volume and pore size. The presence of certain lattice defects proves beneficial in enhancing the light-harnessing effect of TiO₂ [36].

By assessing the rate at which MG degrades under 120 min of visible light irradiation, the CdS- and C₆₀-co-modified TiO₂ samples can be evaluated for their visible light catalytic activity. They were put through photocatalytic degradation tests with commercial P25 under identical circumstances to assess their photocatalytic activity. The UV absorption spectra of CdS, CdS-C₆₀, CdS-TiO₂, and CdS-C₆₀/TiO₂ are displayed in Figure 3a–d. These spectra demonstrate that the absorbance values decrease with an increasing visible light irradiation period, indicating a significant and quick degradation of MG. To examine the kinetics of MG's photocatalytic breakdown in more detail, we measured the photocatalytic degradation curves of five catalyst samples, as shown in Figure 3e–f [37]. According to the relevant formula, we calculated the apparent rate constant k_{app} for the catalytic reactions with different catalysts in Table S1 (Supporting information), and it was indicated that the photocatalytic efficiency of all the samples was significantly higher than that of P25 when

exposed to visible light. The order of photocatalytic efficiency was $\text{CdS-C}_{60}/\text{TiO}_2 > \text{CdS-C}_{60} > \text{CdS} > \text{CdS-TiO}_2 > \text{P25}$. It can be seen that the composite materials have significant catalytic activity. Compared with the pure materials, the catalytic activity of the C_{60} -modified materials is improved due to C_{60} 's ability to enhance the quantum efficiency and facilitate charge transfer: C_{60} can enhance the efficiency of separating photogenerated e^- - h^+ pairs. Meanwhile, it can also enhance the adsorption efficiency during the degradation process [38,39]. This is also due to the small band gap width (2.4 eV) of CdS, which can induce photocatalysis in the visible light region. CdS can provide excited e^- to TiO_2 , while water and oxygen are used to generate hydroxyl radicals ($\cdot\text{OH}$) and superoxide anion radicals ($\cdot\text{O}_2^-$). These free radicals contribute to the photooxidation of the adsorbed organic matrix. The $\text{CdS-C}_{60}/\text{TiO}_2$ sample exhibits both the characteristics of C_{60} and CdS, thus exhibiting the highest photocatalytic activity.

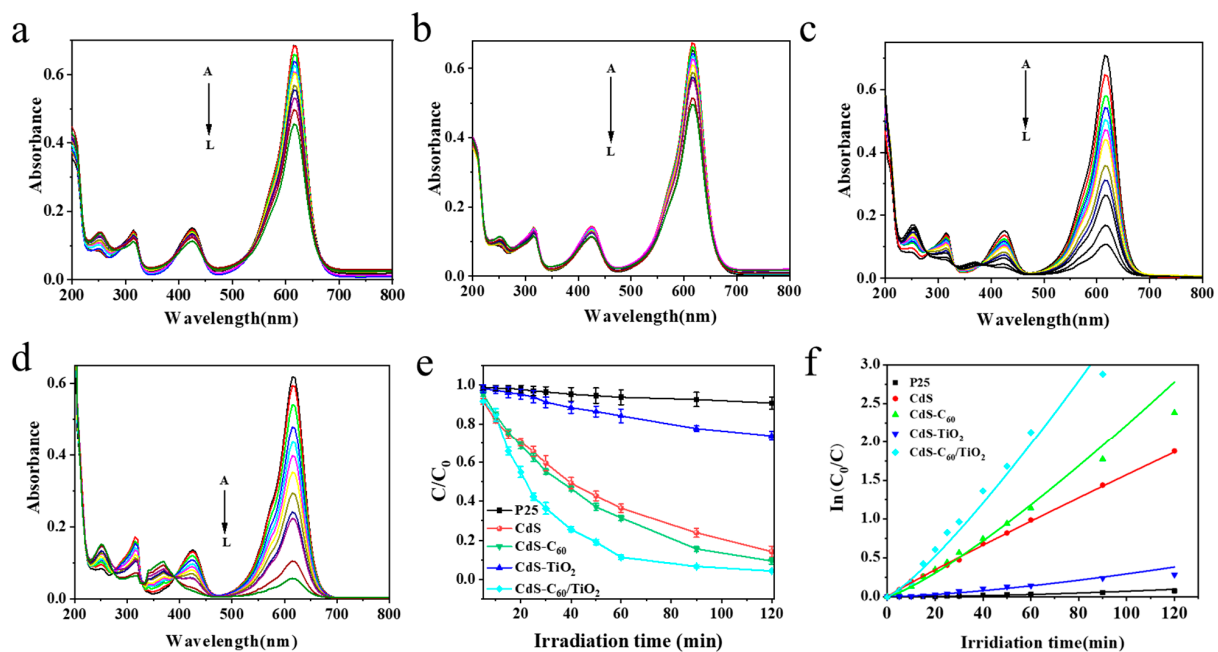


Figure 3. Spectrum of adsorption of MG solution in the presence of (a) CdS; (b) CdS-TiO₂; (c) CdS-C₆₀; and (d) CdS-C₆₀/TiO₂ under different irradiation times when exposed to halogen tungsten lamp. For A–G, each absorbance spectrum was recorded over a 5 min interval; for G–J, each absorbance spectrum was recorded over a 10 min interval; for J–L, each absorbance spectrum was recorded over a 30 min interval with visible light illumination. (e) Absorbance variations as a function of irradiation time (f), $\ln(c_0/c)$, and the linear of control for P25, CdS, CdS-C₆₀, CdS-TiO₂, CdS-C₆₀/TiO₂ in MG deterioration after 120 min exposure to radiation at ambient temperature. [MG] = 4 mg/L; [P25] (CdS, CdS-C₆₀, CdS-TiO₂, CdS-C₆₀/TiO₂) = 0.6 g/L.

Moreover, we conducted adsorption mechanical analysis on the different catalysts. The pore size and pore distribution can be calculated in Table S2 (Supporting Information). The factors influencing the photocatalytic performance of the sample are connected to the combined impact of an appropriate specific surface area and a certain level of lattice defects, which is beneficial for improving the optical effect of TiO₂. The results of our adsorption-based linear fitting analysis are consistent with the desorption equilibrium data for MG using different catalysts, as shown in Figure S4 (Supporting Information). One can enhance the TiO₂ by increasing its specific surface area and modifying its crystal structure; TiO₂ co-modified with C₆₀ can be expected to improve in its photocatalytic performance; and given sufficient time, CdS-C₆₀ is comparable to CdS-C₆₀-TiO₂ in terms of its catalytic performance.

To further analyze the catalytic performance of each catalyst, we conducted a comparison of the photocatalytic hydrogen production yield over time using 10% lactic acid

as a sacrificial reagent. This comparison included various catalysts under visible light conditions, as illustrated in Figure 4a. We tested the average hydrogen production of different catalysts per hour under continuous illumination for 5 h in Figure 4b. As illustrated in Figure 4a,b, the hydrogen production performance of these photocatalysts in order from best to worst is $\text{CdS-C}_{60}/\text{TiO}_2 > \text{CdS-C}_{60} > \text{CdS} > \text{CdS-TiO}_2 = \text{P25}$. The visible light hydrogen production effect of pure P25 and CdS-modified TiO_2 is basically zero, and the average hydrogen production of C_{60} -modified CdS is $5.648 \mu\text{mol/h}$. The photocatalytic activity of CdS when co-modified with TiO_2 and C_{60} is approximately twice as high as that of pure CdS, whereas the average yield of TiO_2 co-modified with CdS and C_{60} is $34.025 \mu\text{mol/h}$, which is roughly 17 times higher than that of pure CdS. The narrow band gap of C_{60} enables the photocatalyst to have a significantly broader absorption band range, thereby enhancing its light absorption capability in the visible light spectrum. C_{60} has good conductivity and can detach photogenerated e^- and promote good separation of the photogenerated $e^- - h^+$, so the visible light hydrogen production performance in CdS can be enhanced through modification with C_{60} . Furthermore, both CdS and C_{60} demonstrate significant light absorption capabilities within the visible spectrum, and C_{60} as an electronic relay can promote the flow of CdS and TiO_2 photogenerated e^- . C_{60} can be used as an active site for photocatalytic hydrogen production, specifically the catalytic cleavage of water to produce H_2 . This indicates that TiO_2 co-modified with CdS and C_{60} has a high photocatalytic activity under visible light conditions.

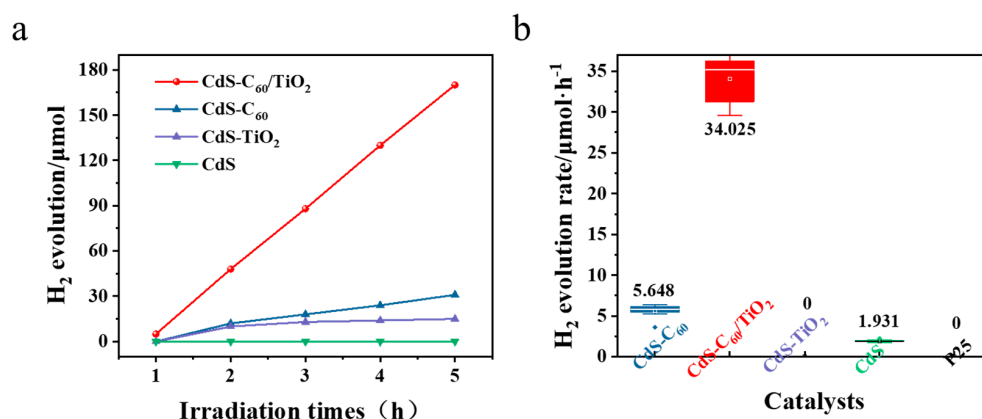


Figure 4. (a) Several kinds of hydrogen production with a time change map; (b) different catalysts per hour of hydrogen production.

A typical impedance equivalent plot is shown in Figure S4a (Supporting Information) to demonstrate the impact of the charge transfer on the activity of catalysts. The EIS Nyquist plots of different catalysts are shown in Figure S5b (Supporting Information). In the Nyquist plots of EIS, the semicircle's diameter shows that CdS, CdS- C_{60} , CdS- TiO_2 , and CdS- $\text{C}_{60}/\text{TiO}_2$ have a lower charge transfer resistance compared to pure TiO_2 . The order of decreasing resistance values is $R(A) < R(B) < R(C) < R(D) < R(E) < R(F)$. It can speed up the charge separation and promote e^- transfer. This helps to decrease the likelihood of recombining $e^- - h^+$ pairs and enhances the photocatalytic activity [40–42]. From the results of electrochemical AC impedance, we see the effective charge transfer rate of CdS is weaker than that of CdS- TiO_2 , but in the photodegradation experiment, the photodegradation rate is higher than that of CdS- TiO_2 . The possible reasons for this are that CdS can provide excitation of e^- to TiO_2 ; within 18 h after the modification of the empty gold sheet, the pure CdS is unstable on its own, and it may have developed photocorrosion, which, in turn, reduced the conductivity.

To illustrate the photodegradation mechanism of the catalyst CdS- $\text{C}_{60}/\text{TiO}_2$, we give a schematic diagram of the corresponding photodegradation mechanism, as shown in Figure 5. On the one hand, C_{60} has a good electron transport performance, which can accelerate the photoinduced charge separation and slow down charge recombination. Under

natural light irradiation, the valence electrons (e^-) in TiO_2 are excited to the conduction band (CB), and holes (h^+) are generated in the valence band (VB). However, these photo-generated electrons–holes can recombine quickly in the photocatalytic reaction, but since C_{60} is a good electron acceptor and can receive electrons from the titanium dioxide, the lifetime of the photogenerated e^- and h^+ will be extended during the transfer process. The photogenerated h^+ can form hydroxyl radicals, with a strong oxidizing activity and OH^- adsorbed on the surface of the TiO_2 . The photogenerated e^- form oxyanion radicals with the oxygen molecules adsorbed on the surface of the TiO_2 , which can effectively photolyze organic radicals or water under the action of free radicals. The resulting active substances ($\bullet\text{O}^{2-}$ and $\bullet\text{OH}$) have a high degradation activity for MG.

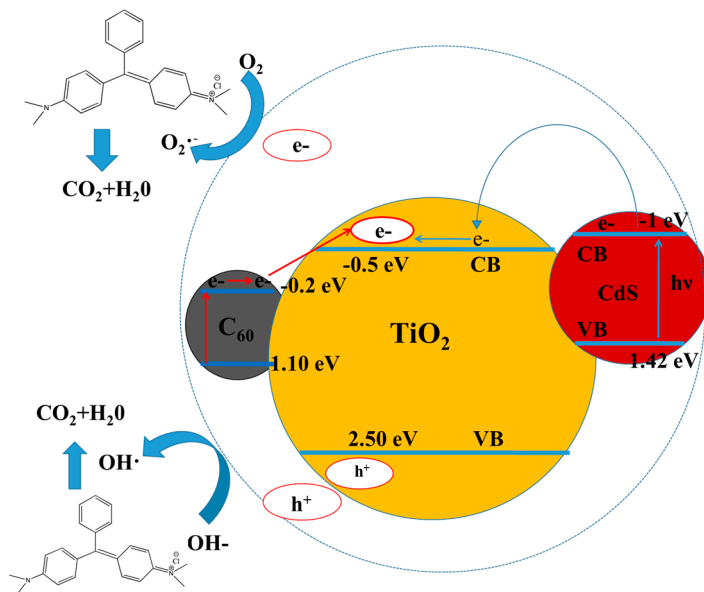


Figure 5. The photodegradation mechanism schematic for $\text{CdS-C}_{60}\text{-TiO}_2$.

On the other hand, TiO_2 and CdS can transition under illumination simultaneously, with the latter's conduction band position being higher than the former, so there is a misalignment of the two in the schematic diagram of the mechanism. Generally, when TiO_2 absorbs light with an energy greater than its band gap, the e^- in the valence band can be excited and move to the conduction band. This leads to the formation of highly active e^- in the conduction band and corresponding h^+ in the valence band [43]. The photogenerated e^- and h^+ are separated and moved toward the surface of the semiconductor particles due to the presence of an electric field, causing highly active photogenerated e^- - h^+ pairs. This indicates that the transition of the electrons from the excited state of CdS to the conduction band of TiO_2 occurs, and then these e^- are absorbed by O_2 molecules to form the superoxide anion radical $\text{O}_2^{\bullet-}$ [44–46]. Consequently, the adsorbed organic matrix's photooxidation characteristics are improved by this shift in vector transfer, to effectively enhance the photooxidation performance of the adsorbed organic matrix. Due to the photogenerated h^+ 's valence potential, which prevents them from oxidizing hydroxyl groups into hydroxyl radicals, CdS photocorrodes to create Cd^{2+} . In short, both C_{60} and CdS components enhance the catalytic effect of TiO_2 ; therefore, $\text{CdS-C}_{60}/\text{TiO}_2$ exhibits a high catalytic activity.

4. Conclusions

In summary, the preparation of CdS - and C_{60} -co-modified TiO_2 photocatalysts via the sol-gel method was followed by their comprehensive characterization using various techniques. Our rigorous investigation into their photocatalytic performance and hydrogen production capacity showcased the exceptional effectiveness of the ternary composite catalyst $\text{CdS-C}_{60}/\text{TiO}_2$ in oxidizing the targeted degradants. The results demonstrated

the impressive average hydrogen production of 34.025 $\mu\text{mol/h}$ for TiO_2 co-modified with CdS and C_{60} , marking a substantial 17-fold increase when compared to pure CdS. In parallel, the average hydrogen generation for C_{60} -modified CdS surged to 5.648 $\mu\text{mol/h}$, representing a notable two-fold enhancement over pure CdS. This remarkable performance can be attributed to the collaborative impact of CdS and C_{60} , which displayed synergistic effects when combined with TiO_2 . The co-modifying strategy effectively minimized the likelihood of photogenerated electron–hole recombination while simultaneously reducing the material’s band gap. These findings underscore the vast potential of CdS- C_{60} / TiO_2 as a high-performance photocatalytic system, with versatile application fields such as renewable energy and environmental remediation. We have compiled a comprehensive overview of highly efficient catalysts for the degradation of MG (refer to Table S3 in the Supporting Information). Although our designed catalysts may not exhibit an optimal performance, our work offers a practical approach to enhancing the effectiveness of photocatalytic degradation by utilizing novel ternary materials.

Supplementary Materials: The following supporting information can be downloaded at <https://www.mdpi.com/article/10.3390/ma17051206/s1>. Figures S1–S5: XPS, SEM, TEM, N_2 adsorption and desorption isotherms and pore size distributions and electrochemical impedance spectroscopy measurement of different samples; Tables S1–S3: Kinetics parameters of photocatalytic degradation of MG, physical parameters of the adsorption and the photocatalytic degradation of MG at different catalysts. References [47–55] are cited in the supplementary materials.

Author Contributions: Y.L. and M.Z. conceived the idea and performed the experiments. X.L. and Y.G. contributed to the interpretation of the results. X.L. and M.Z. wrote and revised the manuscript. All authors discussed the results and commented on the manuscript. All authors have read and agreed to the published version of the manuscript.

Funding: We gratefully thank Yuzhang Normal University’s 2021 University-Level Scientific Research Project (Grant No. YZYB-21-16) and the Science and Technology Research Project of Jiangxi Province Education Department (Grant Nos. GJJ213108, 20202ACB202004, 20212BBE53051, 20213BCJ22024) for their financial support.

Institutional Review Board Statement: Not applicable.

Informed Consent Statement: Not applicable.

Data Availability Statement: Data are contained within the article and supplementary materials.

Conflicts of Interest: The authors declare no conflicts of interest.

References

1. Lei, Q.; Yuan, H.; Du, J.; Ming, M.; Yang, S.; Chen, Y.; Lei, J.; Han, Z. Photocatalytic CO_2 reduction with aminoanthraquinone organic dyes. *Nat. Commun.* **2023**, *14*, 1087. [[CrossRef](#)]
2. Huang, W.; Su, C.; Zhu, C.; Bo, T.; Zuo, S.; Zhou, W.; Ren, Y.; Zhang, Y.; Zhang, J.; Rueping, M.; et al. Isolated electron trap-induced charge accumulation for efficient photocatalytic hydrogen production. *Angew. Chem. Int. Ed.* **2023**, *62*, e202304634. [[CrossRef](#)]
3. Barrocas, B.T.; Ambroová, N.; Koí, K. Photocatalytic reduction of carbon dioxide on TiO_2 heterojunction photocatalysts—A review. *Materials* **2022**, *15*, 967. [[CrossRef](#)]
4. Singh, V.; Rao, A.; Tiwari, A.; Yashwanth, P.; Lal, M.; Dubey, U.; Aich, S.; Roy, B. Study on the effects of Cl and F doping in TiO_2 powder synthesized by a sol-gel route for biomedical applications. *J. Phys. Chem. Solids* **2019**, *134*, 262–271. [[CrossRef](#)]
5. Aich, S.; Mishra, M.K.; Sekhar, C.; Satapathy, D.; Roy, B. Synthesis of Al-doped nano Ti-O scaffolds using a hydrothermal route on titanium foil for biomedical applications. *Mater. Lett.* **2016**, *178*, 135–139. [[CrossRef](#)]
6. Caglar, A.; Aktas, N.; Kivrak, H. The role and effect of CdS-based TiO_2 photocatalysts enhanced with a wetness impregnation method for efficient photocatalytic glucose electrooxidation. *Surf. Interfaces* **2022**, *33*, 102250. [[CrossRef](#)]
7. Chen, W.; Tian, Y.; Wang, X.; Ma, R.; Ding, H.; Zhang, H. Preparation and characterization of Zr-containing silica residue purification loaded nano- TiO_2 composite photocatalysts. *Chem. Phys.* **2023**, *570*, 111889. [[CrossRef](#)]
8. Chen, B.C.; Li, P.P.; Wang, B.; Wang, Y.D. Flame-annealed porous $\text{TiO}_2/\text{CeO}_2$ nanosheets for enhanced CO gas sensors. *Appl. Surf. Sci.* **2022**, *593*, 153418. [[CrossRef](#)]
9. Chen, Y.J.; Luo, X.; Luo, Y.; Xu, P.W.; He, J.; Jiang, L.; Li, J.J.; Yan, Z.Y.; Wang, J.Q. Efficient charge carrier separation in l-alanine acids derived N- TiO_2 nanospheres: The role of oxygen vacancies in tetrahedral Ti^{4+} sites. *Nanomaterials* **2019**, *9*, 698. [[CrossRef](#)] [[PubMed](#)]

10. Deng, L.; Liu, Y.; Zhao, G.; Chen, J.H.; He, S.F.; Zhu, Y.C.; Chai, B.; Ren, Z.D. Preparation of electrolyzed oxidizing water by TiO₂ doped IrO₂-Ta₂O₅ electrode with high selectivity and stability for chlorine evolution. *J. Electroanal. Chem.* **2019**, *832*, 459–466. [[CrossRef](#)]
11. Li, S.Q.; Li, J.Z.; Zhang, H.X.; Luo, B.; Cai, H.; Nie, S.X.; Sha, J.L. Ultraviolet-light-driven electricity generation by a TiO₂/graphene composite in water. *ACS Mater. Lett.* **2023**, *5*, 2862–2869. [[CrossRef](#)]
12. Li, G.Q.; Xu, T.; He, R.F.; Li, C.P.; Bai, J. Hollow cadmium sulfide tubes with novel morphologies for enhanced stability of the photocatalytic hydrogen evolution. *Appl. Surf. Sci.* **2019**, *495*, 143642. [[CrossRef](#)]
13. Goud, B.S.; Suresh, Y.; Annapurna, S.; Singh, A.K.; Bhikshamaiah, G. Green synthesis and characterization of cadmium sulphide nanoparticles. *Mater. Today Proc.* **2016**, *3*, 4003–4008. [[CrossRef](#)]
14. Jang, J.S.; Kim, H.G.; Joshi, U.A.; Jang, J.W.; Lee, J.S. Fabrication of CdS nanowires decorated with TiO₂ nanoparticles for photocatalytic hydrogen production under visible light irradiation. *Int. J. Hydrogen Energ.* **2008**, *33*, 5975–5980. [[CrossRef](#)]
15. Ma, J.Y.; An, Z.H.; Zhang, W.W.; Shen, J.; Qi, Y.L.; Chen, D.H. TiO₂/CdS composite photocathode improves the performance and degradation of wastewater in microbial fuel cells. *Anal. Sci. Adv.* **2022**, *3*, 188–197. [[CrossRef](#)]
16. Huo, G.N.; Zhang, S.S.; Li, Y.L.; Li, J.X.; Zhao, Y.; Huang, W.P.; Zhang, S.M.; Zhu, B.L. CdS-modified TiO₂ nanotubes with heterojunction structure: A photoelectrochemical sensor for glutathione. *Nanomaterials* **2023**, *13*, 13. [[CrossRef](#)] [[PubMed](#)]
17. Xing, Z.; Li, S.H.; Hui, Y.; Wu, B.S.; Chen, Z.C.; Yun, D.Q.; Deng, L.L.; Zhang, M.L.; Mao, B.W.; Xie, S.Y.; et al. Star-like hexakis[di(ethoxycarbonyl)methano]-C₆₀ with higher electron mobility: An unexpected electron extractor interfaced in photo-voltaic perovskites. *Nano Energy* **2020**, *774*, 104859. [[CrossRef](#)]
18. Zieleniewska, A.; Lodermeier, F.; Rotha, A.; Guldi, D.M. Fullerenes-how 25 years of charge transfer chemistry have shaped our understanding of (interfacial) interactions. *Chem. Soc. Rev.* **2018**, *47*, 702–714. [[CrossRef](#)] [[PubMed](#)]
19. Xia, D.; Zhang, Z.; Zhao, C.; Wang, J.; Li, W. Fullerene as an additive for increasing the efficiency of organic solar cells to more than 17%. *J. Colloid Interf. Sci.* **2021**, *601*, 70–77. [[CrossRef](#)] [[PubMed](#)]
20. Fang, Y.; Wei, Z.Y.; Guan, Z.H.; Shan, N.Y.; Zhao, Y.; Liu, F.; Fu, L.L.; Huang, Z.P.; Humphrey, M.G.; Zhang, C. Covalent chemical functionalization of Ti₃C₂T_x MXene nanosheets with fullerenes C₆₀ and C₇₀ for enhanced nonlinear optical limiting. *J. Mater. Chem. C* **2023**, *11*, 7331–7344. [[CrossRef](#)]
21. Kang, S.; Bozhilov, K.; Myung, N.; Mulchandani, A.; Chen, W. Microbial Synthesis of CdS Nanocrystals in Genetically Engineered *E. coli*. *Angew. Chem. Int. Ed.* **2008**, *47*, 5186–5189. [[CrossRef](#)]
22. Xu, M.; Kang, Y.; Jiang, L.; Jiang, L.; Tremblay, P.; Zhang, T. The one-step hydrothermal synthesis of CdS nanorods modified with carbonized leaves from Japanese raisin trees for photocatalytic hydrogen evolution. *Int. J. Hydrogen Energy* **2022**, *47*, 15516–15527. [[CrossRef](#)]
23. Li, X.H.; Li, Y.J.; Guo, X.; Jin, Z.L. Design and synthesis of ZnCo₂O₄/CdS for substantially improved photocatalytic hydrogen production. *Front. Chem. Sci. Eng.* **2023**, *17*, 606–616. [[CrossRef](#)]
24. Li, J.L.; Xu, X.T.; Liu, X.J.; Qin, W.; Wang, M.; Pan, L.K. Metal-organic frameworks derived cake-like anatase/rutile mixed phase TiO₂ for highly efficient photocatalysis. *J. Alloys Compd.* **2017**, *690*, 640–646. [[CrossRef](#)]
25. Zhang, K.L.; Liu, C.M.; Huang, F.Q.; Zheng, C.; Wang, W.D. Study of the electronic structure and photocatalytic activity of the BiOCl photocatalyst. *Appl. Catal. B Environ.* **2006**, *68*, 125–130. [[CrossRef](#)]
26. Li, Y.; Jiang, J.W. Modulation of thermal conductivity of single-walled carbon nanotubes by fullerene encapsulation: The effect of vacancy defects. *Phys. Chem. Chem. Phys.* **2023**, *11*, 7734–7740. [[CrossRef](#)] [[PubMed](#)]
27. Zhou, W.R.; Jia, L.B.; Chen, M.Q.; Li, X.C.; Su, Z.H.; Shang, Y.B.; Jiang, X.F.; Gao, X.Y.; Chen, T.; Wang, M.T.; et al. An improbable amino-functionalized fullerene spacer enables 2D/3D hybrid perovskite with enhanced electron transport in solar cells. *Adv. Funct. Mater.* **2022**, *32*, 2201374. [[CrossRef](#)]
28. Brik, M.G.; Srivastava, A.M.; Popov, A.I. A few common misconceptions in the interpretation of experimental spectroscopic data. *Opt. Mater.* **1992**, *32*, 249–253. [[CrossRef](#)]
29. Zhou, X.A.; Ye, S.T.; Zhao, S.F.; Song, H.H.; Gong, H.T.; Fan, S.R.; Liu, M.J.; Wang, M.L.; Zhou, W.H.; Liu, J.J.; et al. Unraveling structure sensitivity in the photocatalytic dehydrogenative C-C coupling of acetone to 2,5-Hexanedione over Pt/TiO₂ catalysts. *ACS Catal.* **2023**, *13*, 11825–11833. [[CrossRef](#)]
30. Hu, S.; Qiao, P.Z.; Zhang, L.P.; Jiang, B.J.; Gao, Y.T.; Hou, F.; Wu, B.G.; Li, Q.; Jiang, Y.; Tian, C.G.; et al. Assembly of TiO₂ ultrathin nanosheets with surface lattice distortion for solar-light-driven photocatalytic hydrogen evolution. *Appl. Catal. B* **2018**, *239*, 317–323. [[CrossRef](#)]
31. Sambur, J.; Brgoch, J. Unveiling the hidden influence of defects via experiment and data science. *Chem. Mater.* **2023**, *35*, 7351–7354. [[CrossRef](#)]
32. Wang, X.; Liu, Y.; Arandiyani, H.; Yang, H.; Bai, L.; Mujtaba, J.; Wang, Q.; Liu, S.; Sun, H. Uniform Fe₃O₄ microflowers hierarchical structures assembled with porous nanoplates as superior anode materials for lithium-ion batteries. *Appl. Surf. Sci.* **2016**, *389*, 240–246. [[CrossRef](#)]
33. Rahmati, M.S.; Fazaeli, R.; Saravani, M.G.; Ghiasi, R. Cu-curcumin/MCM-41 as an efficient catalyst for in situ conversion of carbazole to fuel oxygenates: A DOE approach. *J. Nanostruct. Chem.* **2022**, *12*, 307–327. [[CrossRef](#)]
34. Yan, J.; Liu, X.L.; Wang, X.T.; Wang, L.J.; Weng, W.S.; Yu, X.T.; Xing, G.B.; Xie, J.; Lu, C.; Luo, Y.; et al. Influence of nano-attapulgitite on compressive strength and microstructure of recycled aggregate concrete. *Cem. Concr. Comp.* **2022**, *134*, 104788. [[CrossRef](#)]

35. Kanjan, N.; Laokul, P.; Maiaugree, W. Photocatalytic activity of nanocrystalline Fe³⁺-doped anatase TiO₂ hollow spheres in a methylene blue solution under visible-light irradiation. *J. Mater. Sci. Mater. Electron.* **2022**, *33*, 4659–4680. [[CrossRef](#)]
36. Mohajernia, S.; Andryskova, P.; Zoppellaro, G.; Kment, S.; Zboril, R.; Schmidt, J.; Schmuki, P. Influence of Ti³⁺ defect-type on heterogeneous photocatalytic H₂ evolution activity of TiO₂. *J. Mater. Chem. A.* **2020**, *8*, 1432–1442. [[CrossRef](#)]
37. Belghiti, M.; Tanji, K.; El Mersly, L.; Lamsayety, I.; Ouzaouit, K.; Faqir, H.; Benzakour, I.; Rafqah, S.; Outzourhit, A. Fast and non-selective photodegradation of basic yellow malachite green, tetracycline, and sulfamethazine using a nanosized ZnO synthesized from zinc ore. *React. Kinet. Mech. Cat.* **2022**, *135*, 2265–2278. [[CrossRef](#)]
38. Causa, M.; Risse, J.D.J.; Scarongella, M.; Brauer, J.C.; Domingo, E.B.; Moser, J.E.; Stingelin, N.; Banerji, N. The fate of electron-hole pairs in polymer: Fullerene blends for organic photovoltaics. *Nat. Commun.* **2016**, *7*, 12556. [[CrossRef](#)]
39. Katal, R.; Farahan, M.H.D.A.; Hu, J.Y. Degradation of acetaminophen in a photocatalytic (batch and continuous system) and photoelectrocatalytic process by application of faceted-TiO₂. *Sep. Purif. Technol.* **2020**, *230*, 115859. [[CrossRef](#)]
40. Low, J.; Yu, J.; Jaroniec, M.; Wageh, S.; Al-Ghamdi, A.A. Heterojunction photocatalysts. *Adv. Mater.* **2017**, *29*, 160694. [[CrossRef](#)] [[PubMed](#)]
41. Nagappagari, L.R.; Le, T.D.; Ahemad, M.J.; Oh, G.J.; Shin, G.S.; Lee, K.Y.; Yu, Y.T. Enhancement of bifunctional photocatalytic activity of boron-doped g-C₃N₄/SnO₂ heterojunction driven by plasmonic Ag quantum dots. *Mater. Today Nano* **2023**, *22*, 100325. [[CrossRef](#)]
42. Islam, M.R.; Chakraborty, A.K.; Gafur, M.A.; Rahman, M.A.; Rahman, M.H. Easy preparation of recyclable thermally stable visible-light-active graphitic-C₃N₄/TiO₂ nanocomposite photocatalyst for efficient decomposition of hazardous organic industrial pollutants in aqueous medium. *Res. Chem. Intermed.* **2019**, *45*, 11753–11773. [[CrossRef](#)]
43. Truc, N.T.T.; Pham, T.D.; Nguyen, M.V.; Thuan, D.V.; Trung, D.Q.; Thao, P.; Trang, H.T.; Nguyen, V.N.; Tran, D.T.; Minh, D.N.; et al. Advanced NiMoO₄/g-C₃N₄ Z-scheme heterojunction photocatalyst for efficient conversion of CO₂ to valuable products. *J. Alloys Compd.* **2020**, *842*, 155860. [[CrossRef](#)]
44. Boettche, S.W.; Oene, S.Z.; Lonerga, M.C.; Surendranat, Y.; Ardo, S.; Broze, C.; Kempler, P.A. Potentially confusing: Potentials in electrochemistry. *ACS Energy Lett.* **2021**, *6*, 261–266. [[CrossRef](#)]
45. Pasarán, A.C.; Luke, T.L.; Zarazúa, I.; Rosa, E.D.; Ramírez, R.F.; Sanal, K.C.; Ordaz, A.A. Co-sensitized TiO₂ electrodes with different quantum dots for enhanced hydrogen evolution in photoelectrochemical cells. *J. Appl. Electrochem.* **2019**, *49*, 475–484. [[CrossRef](#)]
46. Mao, Z.; Lin, H.; Xu, M.; Miao, J.; He, S.J.; Li, Q. Fabrication of Co-doped CdSe quantum dot-sensitized TiO₂ nanotubes by ultrasound-assisted method and their photoelectrochemical properties. *J. Appl. Electrochem.* **2018**, *48*, 147–155. [[CrossRef](#)]
47. Oh, W.C.; Zhang, F.J.; Chen, M.L. Preparation of MWCNT/TiO₂ composites by using MWCNTs and titanium (IV) alkoxide precursors in benzene and their photocatalytic effect and bactericidal activity. *Bull. Korean Chem. Soc.* **2009**, *30*, 2637–2642.
48. Li, Y.S.; Jiang, F.L.; Xiao, Q.; Li, R.; Li, K.; Zhang, M.F.; Zhang, A.Q.; Sun, S.F.; Liu, Y. Enhanced photocatalytic activities of TiO₂ nanocomposites doped with water-soluble mercapto-capped CdTe quantum dots. *Appl. Catal. B* **2010**, *101*, 118–129. [[CrossRef](#)]
49. Al-Ekabi, H.; Serpone, N. Kinetic studies in heterogeneous photocatalysis. 1. Photocatalytic degradation of chlorinated phenols in aerated aqueous solutions over TiO₂ supported on a glass matrix. *J. Phys. Chem.* **1988**, *92*, 5726–5731. [[CrossRef](#)]
50. Al-Ekabi, H.; Serpone, N.; Wang, X.H.; Li, J.G.; Kamiyama, H.; Moriyoshi, Y.; Ishigaki, T. Wavelength-sensitive photocatalytic degradation of methyl orange in aqueous suspension over Iron(III) doped TiO₂ nanopowders under UV and visible light irradiation. *J. Phys. Chem. B* **2006**, *110*, 6804–6809.
51. Korshin, G.; Chow, C.W.K.; Fabris, R.; Drikas, M. Absorbance spectroscopy-based examination of effects of coagulation on the reactivity of fractions of natural organic matter with varying apparent molecular weights. *Water Res.* **2009**, *43*, 1541–1548. [[CrossRef](#)] [[PubMed](#)]
52. Halomoan, I.; Yulizar, Y.; Surya, R.M.; Apriandanu, D.O. Facile preparation of CuO-Gd₂Ti₂O₇ using acmella uliginosa leaf extract for photocatalytic degradation of malachite green. *Mater. Res. Bull.* **2022**, *150*, 111726. [[CrossRef](#)]
53. Jia, J.; Du, X.; Surya, R.M.; Zhang, Q.Q.; Liu, E.Z.; Fan, J. Z-scheme MgFe₂O₄/Bi₂MoO₆ heterojunction photocatalyst with enhanced visible light photocatalytic activity for malachite green removal. *Appl. Surf. Sci.* **2019**, *492*, 527–539. [[CrossRef](#)]
54. Wu, D.; Li, C.; Zhang, D.; Wang, L.; Zhang, X.; Shi, Z.; Lin, Q. Enhanced photocatalytic activity of Gd³⁺ doped TiO₂ and Gd₂O₃ modified TiO₂ prepared via ball milling method. *J. Rare Earths* **2019**, *37*, 845–852. [[CrossRef](#)]
55. Zhang, M.F.; Liang, X.F.; Liu, Y. Co-CNT/TiO₂ composites effectively improved the photocatalytic degradation of malachite green. *Ionics* **2022**, *30*, 521–527. [[CrossRef](#)]

Disclaimer/Publisher's Note: The statements, opinions and data contained in all publications are solely those of the individual author(s) and contributor(s) and not of MDPI and/or the editor(s). MDPI and/or the editor(s) disclaim responsibility for any injury to people or property resulting from any ideas, methods, instructions or products referred to in the content.